NIR-II and visible fluorescence hybrid imaging-guided surgery via aggregation-induced emission fluorophores cocktails

Xiaoxiao Fan [a,b,h,1], Qiming Xia [a,1], Shunjie Liu [c,1], Zheng Zheng [d], Yiyin Zhang [a], Tianxiang Wu [b], Yixuan Li [a], Guping Tang [g], Ben Zhong Tang [f,**], Jun Qian [a,b,***], Hui Lin [a,e,*]

[a] Department of General Surgery, Sir Run Run Shaw Hospital, School of Medicine, Zhejiang University, Hangzhou, 310000, China
[b] State Key Laboratory of Modern Optical Instrumentations, Centre for Optical and Electromagnetic Research, College of Optical Science and Engineering, International Research Center for Advanced Photonics, Zhejiang University, Hangzhou, 310058, China
[c] Key Laboratory of Polymer Ecomaterials, Changchun Institute of Applied Chemistry, Chinese Academy of Sciences, Changchun, 130022, China
[d] School of Chemistry and Chemical Engineering, Hefei University of Technology, Hefei, 230009, China
[e] College of Biomedical Engineering and Instrument Science, Zhejiang University, Hangzhou, 310058, China
[f] Shenzhen Institute of Aggregate Science and Technology, School of Science and Engineering, The Chinese University of Hong Kong, Shenzhen, Guangdong, 518172, China
[g] Department of Chemistry, Zhejiang University, Hangzhou, 310028, China
[h] Guangdong Provincial Key Laboratory of Luminescence from Molecular Aggregates (South China University of Technology), Guangzhou, 510640, China

ARTICLE INFO

ABSTRACT

Fluorescence imaging-guided surgery is one of important techniques to realize precision surgery. Although second near-infrared window (NIR-II) fluorescence imaging has the advantages of high resolution and large penetration depth in surgical navigation, its major drawback is that NIR-II images cannot be detected by our naked eyes, which demands a high hand-eye coordination for surgeons and increases the surgical difficulty. On the contrary, visible fluorescence can be observed by our naked eyes but has poor penetration. Here, we firstly propose a kind of NIR-II and visible fluorescence hybrid navigation surgery assisted via a cocktail of aggregation-induced emission nanoparticles (AIE NPs). NIR-II imaging helps to locate deep targeted tissues and judge the residual, and visible fluorescence offers an easily surgical navigation. We apply this hybrid navigation mode in different animals and systems, and verify that it can accelerate surgical process and compatible with a visible fluorescence endoscopy. To deepen the understanding of lymph node (LN) labelling, the distribution of NPs in LNs after local administration is initially analyzed by NIR-II fluorescence wide-filed microscopy, and two fates of the NPs are summarized. An alternative strategy which combines indocyanine green and berberine is also reported as a compromise for rapidly clinical translation.

1. Introduction

With the development of surgical techniques and skills, surgery has passed through the intuitive and empirical era and entered into the era of precision medicine. [1,2]. In 2013, surgeons started to advocate the concept of precision surgery. [1]. Since then, precision surgery gradually evolves as one of distinctive features of modern surgery and becomes an important part of precision medicine. Its principle is to seek a balance of maximizing resection of all the targeted tissues and maximizing reservation of normal tissues. [2,3]. Maximizing the removal of the targeted lesion aims to ensure therapeutic effect, and maximizing the preservation of normal tissues demands surgeons to control the surgical damage to patients. The emergence of many techniques, such as endoscopic techniques and fluorescence imaging techniques, accelerate the development of precision surgery. [4,5]. Fluorescence imaging-guided surgery perfectly fits the concept of precision surgery. Surgeons can judge the boundary of tumors or diseased tissues by visualizing targeted tissues to ensure complete resection, and maximize organ protection by visualizing normal tissues. Near-infrared (NIR) fluorescence imaging has reached great successes in surgical field. [4,6–8]. It could help to increase the number of lymph node (LN) dissections in laparoscopic gastrectomy, [6],

Abbreviation

NIR-II	second near-infrared window
AIE	aggregation-induced emission
LN	lymph node
NP	nanoparticle
SBR	background ratio
ICG	indocyanine green
DLS	Dynamic light scattering
TEM	transmission electron microscopy
PL	photoluminescence
BSA	bovine serum albumin

facilitate the sentinel LN resection in breast cancer surgery and protect nerves during orthopedic surgery or neurosurgery and so on. [4].

The NIR fluorescence imaging in current surgeries is detecting the fluorescence in NIR-I biological window (760–-900 nm). Imaging in NIR-II biological window (900–-1880 nm) is proven to have a better performance, [9–11], which was first proposed by Dai''s group and subsequently draw great attentions. [10]. In China, Wang and his co-workers firstly started to explore the huge potential of Ag_2S quantum dot in NIR-II imaging in 2012. [12]. It has the advantages of lower autofluorescence, larger penetration depth and higher signal to background ratio (SBR), especially imaging in NIR-IIx window (1400–-1500 nm). [9]. A preliminary attempt has been conducted by Tian et al. to explore the application value of NIR-II imaging in liver tumor resection using indocyanine green (ICG) and proven the great potential of NIR-II imaging in surgical navigation. [13]. However, ICG is the only clinically proven NIR molecule that can be used for NIR-II imaging, and has several drawbacks, such as short blood circulation time, poor optical stability and so on. [13,14]. Developing more NIR-II fluorescent molecules with excellent optical properties is helpful to promote clinical translation of NIR-II imaging. Many fluorescent probes, such as single-walled carbon nanotubes, [10], quantum dots, [15,16], rare-earth doped nanoparticles [17] and organic probes, [18,19], have been designed for NIR-II imaging. Among those fluorescent probes, aggregation-induced emission (AIE) fluorophore is one of potential candidates for clinical translation. Since the concept of AIE proposed in 2001, [20], this field goes through a rapid development. [21–23]. For surgical navigation, it demands that fluorescent probes should be stable, convenient and biocompatibility. AIE fluorophores are known for the high stability, brightness and well biocompatibility, and increasingly become the promising fluorescent probes for biomedical imaging, and thus exhibit great potential in surgical navigation. [24].

A successful fluorescence imaging-guided surgery contains three interrelated elements: fluorescent probes, imaging systems and suitable surgical applications. To data, most of the studies in NIR-II imaging field are mainly focused on the development of fluorescent probes. Previous studies designed different kinds of NIR-II fluorescent probes and explored the application value of NIR-II imaging at an initial stage. [25]. For this reason, the developments of clinical NIR-II imaging systems and its applications in surgery lag behind the rapidly developed fluorescent probes. Our group is dedicated to establishing novel NIR-II imaging systems and expending the potential applications. We previously proposed a multi-channel NIR-II fluorescence imaging-guided surgery mode to facilitate LN resection and protect normal tissues during surgery. [26].

Even though NIR-II imaging has many advantages in imaging-guided surgery, its greatest disadvantage is that it relies on a NIR camera to detect signals. Surgeons should look at a computer screen when performing operations. It demands a high hand-eye coordination for surgeons and undoubtedly prolongs the learning curve. Despite visible fluorescence has a poor penetration, the advantage of visible fluorescence in imaging-guided surgery is that it can be detected by naked eyes

and has a low requirement for equipment, which will significantly accelerate operative speed. A navigation mode combining the advantages of NIR-II fluorescence imaging and visible fluorescence imaging is then in demand. Surgeons can locate and expose the targeted lesion in deep tissues using NIR-II fluorescence imaging and completely resect the lesions under the guidance of visible fluorescence. After the targets are removed, NIR-II fluorescence imaging can be used to examine the residual. Thus, the complementary advantages of NIR-II fluorescence and visible fluorescence can be maximized in imaging-guided surgery.

In this study, we encapsulated TT3-*o*CB, a NIR-II fluorescent AIE probe, and DPBT, a visible fluorescent AIE probe, with pluronic F127 into NPs, respectively. The two kinds of AIE NPs were then mixed up to form a cocktail of AIE NPs. Based on it, we firstly reported a kind of NIR-II and visible fluorescence hybrid navigation mode and applied this navigation mode in different experimental animals (mouse, rat and rabbit) and different systems (LN, bile duct and ureter). The standard procedure of hybrid fluorescence imaging-guided surgery was suggested to contain six steps to ensure the accurate and complete resection. To deepen the understanding of LN labeling in surgery, the distribution of NPs in LNs was further analyzed by a NIR-II fluorescence wide-field microscope. Also, we proposed that this hybrid navigation mode could use two clinically approved agents, ICG and berberine, as a compromise to realize rapidly clinical translation.

2. Material and methods

2.1. Fabrication and cCharacterization of TT3-oCB NPs and DPBT NPs

The synthesis of TT3-oCB and DPBT molecules were reported in our previous studies. [27,28]. Full details were reported in the Supplementary Information.

2.2. Preparation of berberine chloride@(2-hHydroxypropyl)-β-cyclodextrins

200 mg (2-Hydroxypropyl)-β-cyclodextrins (98%, Aladdin, China) and 59 mg berberine chloride (98%, Aladdin, China) were diluted with the mix solution of ethanol and water (volume ratio = =1:1) and stirred at 65 °C for 24 h hours. Then the ethanol was removed via rotary evaporation at room temperature. The final product, berberine chloride@(2-Hydroxypropyl)-β-cyclodextrins, was obtained by drying the mixed solution using lyophilization.

2.3. Mixed tracers

Because InGaAs camera was very sensitive, the autofluorescence in visible light region was more obvious and TT3-oCB materials could absorb the fluorescence emitted by DPBT materials, the concentration of DPBT NPs (0.8 mg/mL) was 4 times higher than that of TT3-*o*CB NPs (0.2 mg/mL) in AIE NPs cocktail (TT3-*o*CB: DPBT = 1: 4). The alternative mixture consisted of ICG (0.2 mg/mL) and berberine chloride@ (2-Hydroxypropyl)-β-CD (contained 2 mg/mL berberine chloride).

2.4. The measurement of absorption and PL spectra

Absorption spectra were recorded with a Shimadzu UV-2550 scanning spectrophotometer (Shimadzu, Japan). PL spectra of DPBT@F127, berberine, and berberine@β-cyclodextrin were detected with a F-2500 fluorescence spectrophotometer (Hitachi, Japan). PL spectra of TT3-oCB@F127 and ICG were detected with a home-built lateral NIR fluorescence receiving system consisting of a 690 nm Laser, a 750 nm long-pass filter and an NIR2200 spectrometer (Ideaoptics, China).

2.5. Animals and LN metastasis model

ICR mice (6–-7 weeks), Rats (200 g), and New Zealand rabbits (1.5–-

2 kg) were purchased from the Laboratory of Animal Center of Sir Run Run Shaw Hospital of Zhejiang University School of Medicine. All the animal protocols were conducted under approved protocols from the Animal Laboratory Ethics Committee of Sir Run Run Shaw Hospital, Zhejiang University. Anesthesia and analgesics were used for all the animals prior to and during the experimental interventions to minimize any suffering of the animals.

To establish the axillary LN metastasis model, $5 \times \times 10^5$ luciferase-transfected 4T1 cells were suspended in 20 μl PBS and further injected into the fore foot pad of mouse. The luciferase signals of axillary LNs were detected at 7 day post-injection.

2.6. In vivo NIR-II & visible fluorescence imaging system

The in vivo NIR-II & visible fluorescence imaging system consisted of an NIR-II fluorescence imaging system which was described in our previous study [26] and an ultraviolet lamp. The beam of 808 nm laser was coupled to a collimator and expanded by a lens, providing uniform irradiation on the imaging flied. Initially, a fixed focal lens was used to collect the signals and an InGaAs camera (SW640, Tekwin, Xi''an, China) was utilized to detect the NIR-II fluorescence signals through a 1100 nm long-pass filter or 1400 nm long-pass filter (Thorlabs, USA). Later, the ultraviolet lamp was manipulated as the light source, and the visible fluorescence could be witnessed with the naked eye or a CCD camera.

2.7. NIR-II wWide-field microscopic fluorescence imaging of LNs

Resected LNs were collected and adhered to cover slides, and then observed by a NIR-II fluorescence wide-field microscope (NIR II-MS, Sunny Optical Technology, Ningbo, China). The 808 nm laser was used as the excitation source, which passed through the objective (XLPLN25XWMP2, 25 × ×, numerical aperture (NA) = =1.05, Olympus, Japan) after being reflected by the dichroic mirror (DMLP900R, Thorlabs, USA). The fluorescence signals were detected by an InGaAs camera (SD640, Tekwin, Xi''an, China).

2.8. Visible fluorescence endoscope

The visible fluorescence endoscope was modified based on a commercial micro-endoscope (LOK VIEW, Shen Zhen, China). The images obtained during endoscopy were recorded using a CCD camera (LOK VIEW, Shen Zhen, China) through a 400 nm long-pass filter and a 750 nm short-pass filter. A 390 nm laser was also introduced into endoscope to excite visible fluorescence.

2.9. Statistical analysis

Quantitative image analysis was accomplished by Image J software (1.8.0, National Institutes of Health, USA). Graphs were generated by Graphpad Prism (Graphpad Prism 8.3.0, Graphpad Software, USA). Statistical analysis was performed using SPSS (SPSS 20.0 version, SPSS Inc., Chicago, USA). Student''s t-test was conducted to assess the differences between different groups. A p-value < 0.05 was considered statistically significant.

3. Results and dDiscussion

3.1. Characterizations of TT3-oCB NPs and DPBT NPs and LNs imaging via aggregation-induced emission nanoprobes cocktail in mice

To realize imaging in both NIR-II window and visible light region, we selected two kinds of AIE fluorophores, named TT3-*o*CB and DPBT, respectively. TT3-*o*CB was an AIE fluorophore with a strong NIR-II fluorescence signal, and DPBT was an AIE fluorophore with fluorescence in visible region. The synthesis of both the two molecules were depicted in our previous work. [27,28]. The structural formulas of the two molecules were presented in Supplementary Figure 1. TT3-*o*CB and DPBT were encapsulated with pluronic F127 into NPs, respectively (Fig. 1a and b).

Dynamic light scattering (DLS) analysis showed TT3-*o*CB NPs had an average diameter of 52.7 nm (Supplementary Figure 2), which was consistent with the result of transmission electron microscopy (TEM) (Supplementary Figure 3). The zeta potential of TT3-*o*CB NPs in water was 0.122 mV (Supplementary Figure 4). The absorption peak of TT3-*o*CB NPs occurred at 775 nm (Fig. 1c), and the emission peak was at 1065 nm (Fig. 1d). For DPBT NPs, they had an average diameter of 56.0 nm (Supplementary Figure 5 and 6). The zeta potential of TT3-*o*CB NPs in water was electric neutrality (Supplementary Figure 7). The absorption peak and emission peak of DPBT NPs were at 445 nm (Figs. 1e) and 570 nm (Fig. 1f), respectively. The two NPs were mixed up to form the cocktail of AIE NPs, which could utilize their advantages simultaneously.

We first verified the performance of this AIE NPs cocktail *in vitro* (Fig. 1g–f). Under the excitation of an 808 nm laser, TT3-*o*CB NPs and the AIE NPs cocktail manifested apparent NIR-II signal through a 1100 nm long-pass filter (Fig. 1h). An ultraviolet lamp was used as the excitation light source of DPBT NPs (Supplementary Figure 8). We could easily recognize the orange fluorescence of DPBT NPs and the cocktail with the naked eyes (Fig. 1i). Subsequently, the in vivo experiments were performed in LNs labeling. We injected 50 μL of the cocktail into the forepaw footpad of mice. The axillary lymph node could be clearly distinguished in NIR-II fluorescence imaging beyond 1100 nm wavelength (Fig. 1j, red arrow). By quantitative analysis, the FWHM of the fitting curve in Fig. 1j was calculated as 3.59 mm, and SBR was calculated as 12.89 (Fig. 1k). Under the guidance of NIR-II imaging, we cut open the skin (Fig. 1l), but could not directly observe the LN. Under the ultraviolet lamp excitation, the obvious visible fluorescence from LN could be detected (Fig. 1m). Thanks to the excellently optical properties of DPBT NPs, the excitation power density was very low. Moreover, we mainly utilized the excitation wavelengths of 380--400 nm which were similar to those of the clinically approved 5-aminolevulinic acid (407 nm). Additionally, we injected the cocktail into the rear footpad of mice to visualize the popliteal lymph node (Fig. 1n, red arrow) and into the tail root of the mice to visualize the inguinal lymph node (Fig. 1r, red arrow). The FWHM of the popliteal lymph node was 3.60 mm and SBR was 59.81 (Fig. 1o). The FWHM of the inguinal lymph node was 1.71 mm and SBR was calculated as 10.75 (Fig. 1r, s). After the skin was incised, the invisible popliteal lymph node (Fig. 1p) and inguinal lymph node (Fig. 1t) could be visible under the ultraviolet lamp irradiation (Fig. 1q and u). It demonstrated that such visible fluorescence could provide intuitive guidance to surgeons in the open operation after the targeted tissues were fully exposed.

3.2. Deciphering the distribution of nanoprobes in lymph node by NIR-II fluorescence wide-field microscope

Previous studies, including basic researches and clinical researches, have reported the advantages of NIR fluorescence imaging-guided surgery in LN resection [6,26,29]. It helps surgeons rapidly locate the LN, reduce operative time and increase LN detection rate. Fully exploring the distribution of nanoprobes in LN after local administration will promote further development of this technique and successful clinical translation. However, there are only a few studies focused on the distribution of nanoprobes in LN, and the majority of those studies explored it based on histologic sections [30,31]. For the nanoprobes which phagocytosed by cells, detecting the fluorescent signals in histologic sections can be an accurate method. Whereas for the free nanoprobes in LN, the nanoprobes would be lost and disrupted during the process of section making and staining, which introduces errors into results. Thanks to the larger penetration depth and lower scattering of NIR-II fluorescent signals, our NIR-II fluorescence wide-field microscope could directly decipher the NIR-II signals of nanoprobes in tissues without making tissue sections and thus provide a more accurate method. [32]. Fifteen minutes after injecting TT3-*o*CB NPs into the ICR mice''s fore-foot pad, we harvested
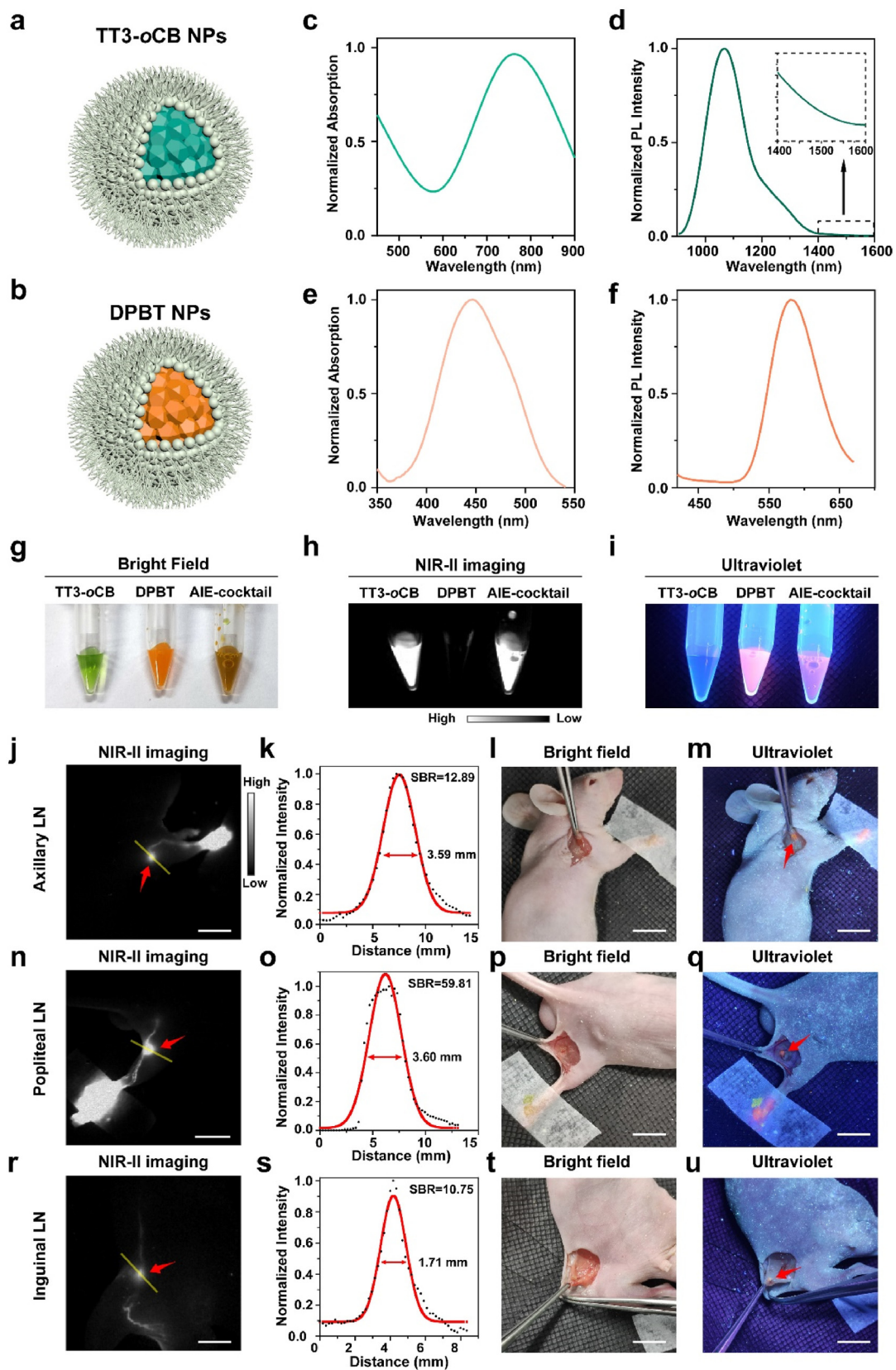
Fig. 1. Schematic illustration of **a)** TT3-*o*CB NPs and **b)** DPBT NPs. **c)** Absorption spectrum and **d)** Photoluminescence (PL) spectrum of TT3-*o*CB NPs. **e)** Absorption spectrum and **f)** PL spectrum of DPBT NPs. Comparison of TT3-*o*CB NPs, DPBT NPs, and the AIE NPs cocktail **g)** under bright field, **h)** under the excitation of an 808 nm laser and **i)** under the excitation of an ultraviolet lamp. NIR-II fluorescence images of **j)** axillary lymph node, **n)** popliteal lymph node and **r)** inguinal lymph node of the nude mice treated with the AIE NPs cocktail (scale bar:1 cm). **k, o, s)** Cross-sectional fluorescence intensity profiles (black) and the Gaussian fits along the yellow lines in (j, n, r). **l, p, t)** the pictures of the areas around the lymph nodes under bright field (scale bar:1 cm). Visible fluorescence signals of the **m)** axillary lymph node, **q)** popliteal lymph node and **u)** inguinal lymph node under the ultraviolet lamp (scale bar:1 cm).

the axillary LN under the guidance of NIR-II camera and placed it on a coverslip (Fig. 2a). Then, LN which adhered to coverslip was directly observed by NIR-II fluorescence wide-field microscope (Fig. 2a). The schematic diagram was presented in Fig. 2b. A layer with uniform fluorescence was detected in every LN (Fig. 2c and Supplementary Figure 9).

Compared with the LN structure, this layer was considered to be the subcapsular sinus. Then, a total of six lymph nodes from ICR mice were harvested for NIR-II fluorescence microscopic imaging after TT3-*o*CB NPs were injected, and the width of subcapsular sinus was measured (Fig. 4d). The mean width of subcapsular sinus was measured as 9.15 ($\pm$
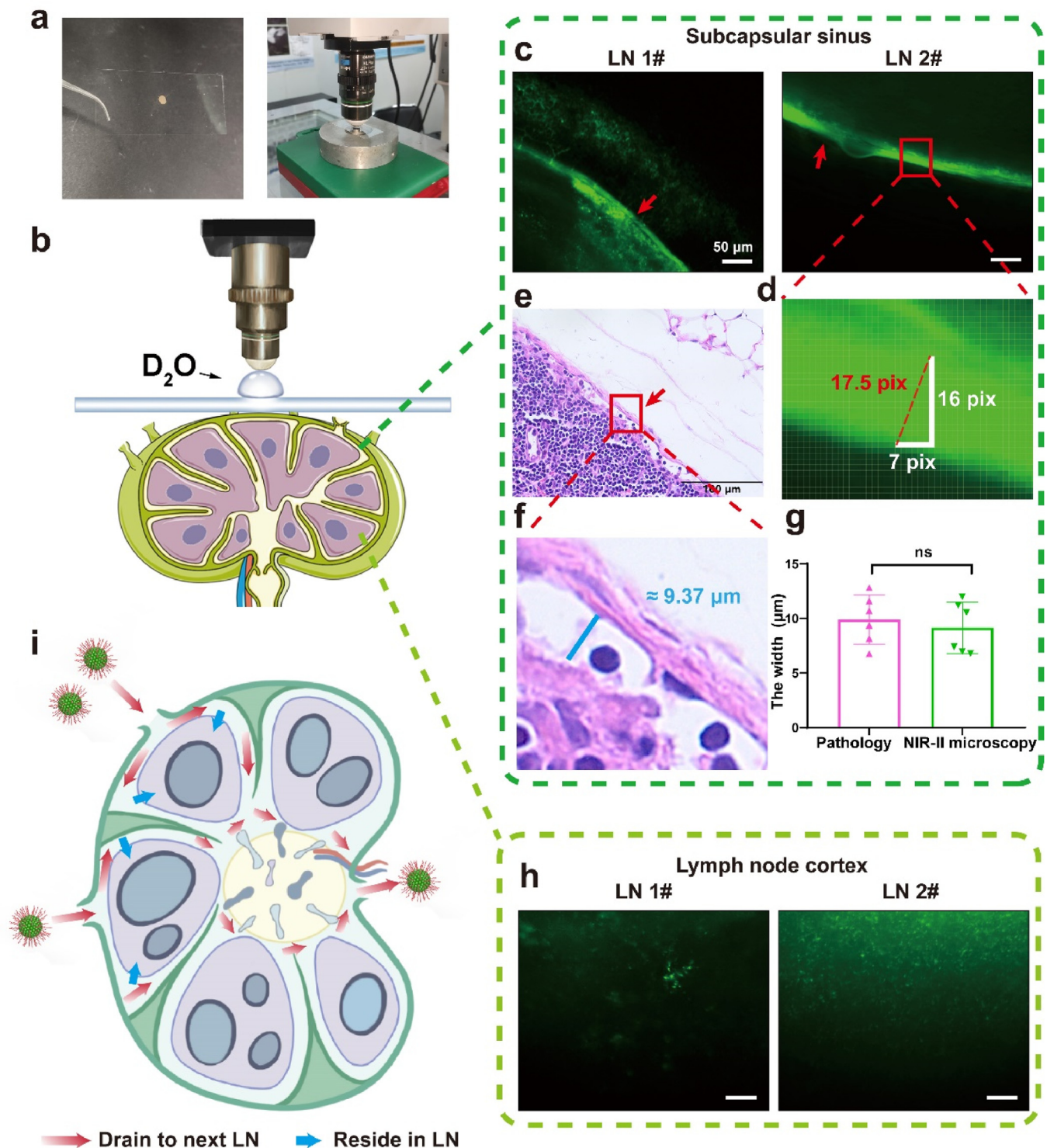

Fig. 2. a) The lymph node adhered to the coverslip was placed on a metal ring-like base under the microscope. b) The schematic diagram of the imaging system and LN structure. c) NIR-II microscopic images of LNs (scale bar: 50 μm). d) The measurement of the width of subcapsular sinus. e) H&E staining of the harvested LN (scale bar: 100 μm). f) The enlarged subcapsular sinus. g) The comparison of the mean width of subcapsular sinus by H&E staining and NIR-II fluorescence optical sectioning. All values are mean $\pm$ S.E.M (standard error of mean) (n = 6). ns, not significant. h) NIR-II microscopic images of the cortexes in the LNs (scale bar: 50 μm). i) The schematic diagram of two fates of NPs in LN.

2.35) μm by the NIR-II optical sectioning method. To further confirm the accuracy of our results, we additionally made pathological sections of six LNs (Fig. 2e and f). There were small gaps between the capsules and LN cortexes which were identified as subcapsular sinuses, and the mean width was measured as 9.89 (± 2.25) μm. The results in pathological level and in optical sectioning level were similar (Fig. 2g). Different from the uniform fluorescent signals in subcapsular sinus, the signals in the LN cortex were divergent (Fig. 2h). It was speculated that those signals were

from the nanoprobes phagocytosed by immune cells in LNs.

Based on our observations through NIR-II optical sectioning, two fates of nanoparticles in LN after injected by local administration were summarized and illustrated in Fig. 2i. Parts of nanoparticles entered into subcapsular sinus, then passed through trabecular sinus and medullary sinus, and finally drained to next LN. Draining in this pathway was usually very fast, and the nanoparticles were in the form of free nanoparticles. The rest parts of nanoparticles were phagocytosed by
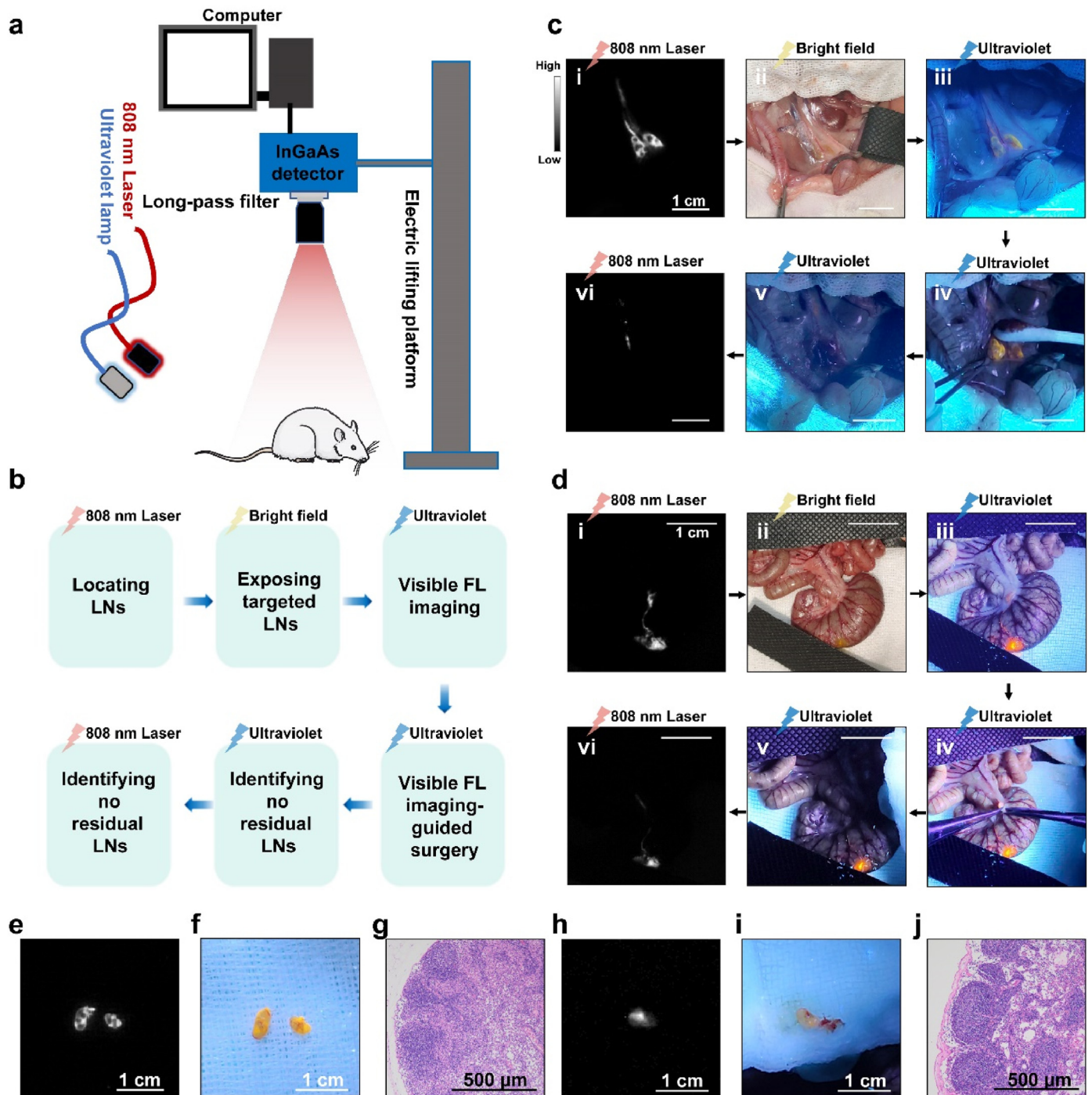

Fig. 3. a) Schematic diagram of NIR-II and visible fluorescence hybrid image-guided navigation system. **b)** Brief description of the six steps in surgery process. **c)** The resection process of the rat's retroperitoneal LNs guided by the AIE NPs cocktail (scale bar: 1 cm). **d)** The resection process of the rat's colon mesenteric LNs guided by the AIE NPs cocktail (scale bar: 1 cm). **e)** NIR-II fluorescence imaging (1400 long-pass filter, exposure time: 50 ms, power intensity: 30 mW/cm^2) and **f)** visible fluorescence imaging of the retroperitoneal LNs (scale bar: 1 cm). **g)** H&E staining of the retroperitoneal LN (scale bar: 500 μm). **h)** NIR-II fluorescence imaging (1400 long-pass filter, exposure time: 50 ms, power intensity: 30 mW/cm^2) and **i)** visible fluorescence imaging of the colon mesenteric LN (scale bar: 1 cm). **j)** H&E staining of the mesenteric LN (scale bar: 500 μm).

subcapsular sinus macrophages and then transferred to LN cortex. Those nanoparticles would reside in the LN and provide persistent fluorescence for LN. Our findings consisted with the previous studies published by Chan et al., which studied the antigen retention and presentation of nanoparticles in LN based on pathological sections. [33]. According to the above-mentioned findings, we emphasized the importance of reserving the intact LN capsules during fluorescence-imaging guided LN resection. On the one hand, keeping the capsules intact helps maintain the bright fluorescence of LN, which assures the sufficient signal intensity of LN during resection. On the other hand, complete capsules can prevent nanoprobes leakage, which may further lead to nanoprobes contamination in the operative region and bring false-positive signals into surgery.

3.3. Standard procedure of NIR-II and visible fluorescence hybrid imaging-guided LN resection

In comparison with mice, the sizes of LNs and the lengths of lymphatic vessels of rats were more comparable to human. We therefore selected rats as experimental animals to validate the practical feasibility of this hybrid surgical navigation mode. A fluorescence imaging-guided intraoperative platform, which consists of a homemade NIR-II fluorescence imaging system, [32], an 808 nm laser and an ultraviolet lamp, was established (Fig. 3a). We suggested that the standard procedure of NIR-II and visible fluorescence hybrid imaging-guided LN resection could be broadly divided into the following six steps: rapidly recognizing the
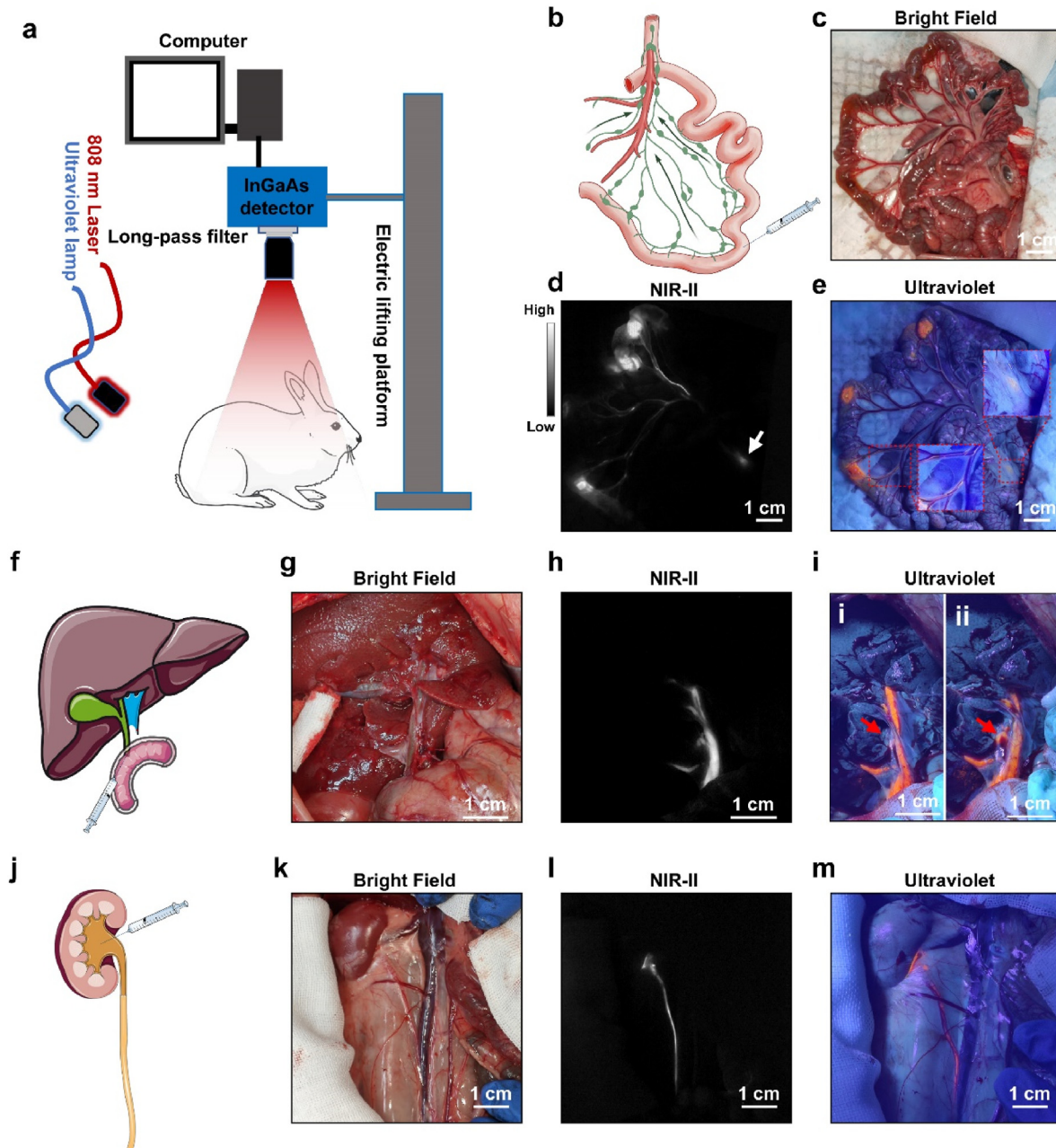

Fig. 4. a) Schematic diagram of hybrid navigation system. **b)** Schematic diagram of rabbit''s mesenteric LNs and injection site. **c)** Morphology of the intestine under bright field (scale bar: 1 cm). **d)** NIR-II fluorescence imaging and **e)** Visible fluorescence imaging of mesenteric LNs and corresponding lymphatic vessels (scale bar: 1 cm). **f)** Schematic diagram of extrahepatic bile ducts and injection site. g) Morphology of the extrahepatic bile ducts under bright field (scale bar: 1 cm). **h)** NIR-II fluorescence imaging and **i)** Visible fluorescence imaging of the extrahepatic bile ducts (scale bar: 1 cm). **j)** Schematic diagram of ureter and renal pelvis injection. **k)** Morphology of the ureter under bright field (scale bar: 1 cm). **l)** NIR-II fluorescence imaging and **m)** Visible fluorescence imaging of the ureter (scale bar: 1 cm). The imaging condition of NIR-II imaging: 1100 long-pass filter, exposure time, 15 ms; power intensity, 15 mW/cm^2.

location of LNs using NIR-II imaging, exposing LNs in bright field under the guidance of NIR-II imaging, identifying the visible fluorescence of LNs under the ultraviolet lamp excitation, imaging-guided LNs resection, confirming there were no residual LNs under the ultraviolet lamp, and further confirming no residual lymph nodes under the 808 nm laser radiation (Fig. 3b). The LNs in posterior peritoneum region and mesocolon were used as our examples. Thirty minutes after the AIE NPs cocktail was injected into the rat''s hindlimb footpad, the retroperitoneal LNs and corresponding lymphatic vessels were clearly visualized in NIR-II imaging under the excitation of an 808 nm laser (Fig. 3c–i). The tissues were dissected and pulled apart gently under the bright field (Fig. 3c–ii). Then, we turned on the ultraviolet lamp, and the visible fluorescence of retroperitoneal LNs could be observed effortlessly with the naked eye (Fig. 3c–iii). Under the guidance of visible fluorescence from LNs, we could remove them accurately and completely (Fig. 3c–iv and Video S1). At last, no residual LNs tissue was confirmed in both visible fluorescence imaging (Fig. 3c–v) and NIR-II fluorescence imaging (Fig. 3c–vi). Similar process was performed to remove the mesenteric lymph nodes of the rat''s colon. In this instance, DPBT and TT3-*o*CB NPs cocktail was injected into the colon wall to trace the mesenteric LN (Fig. 3d) following the above-mentioned six steps. The resected tissues exhibited obvious NIR-II fluorescence signals (Fig. 3e and h) and visible fluorescence signals (Fig. 3f and i), and were confirmed as LNs in pathological level by H&E staining (Fig. 3g and j).

Supplementary data related to this article can be found at https://doi.org/10.1016/j.mtbio.2022.100399.

Because complete removal of suspicious LN metastases could prevent LN recurrence and improve the prognosis, secondary confirmation of thorough excision was thus necessary [34]. This result demonstrated the accuracy and the feasibility of NIR-II and visible fluorescence hybrid imaging-guided surgery via AIE nanoprobes cocktail. Our previous study indicated that imaging beyond 1400 nm wavelength could reach a much better imaging performance [9]. The main mechanism of this phenomenon was because the absorption peak of water at ~1450 nm wavelength could absorb background signals, and thus increased the signal-to-background ratio [9]. We also compared the NIR-II fluorescent images of LNs beyond 1100 nm wavelength (Supplementary Figure 10a) and beyond 1400 nm wavelength (Supplementary Figure 10b). Engrossingly, the internal structures appeared more distinct when using 1400 nm long-pass (LP) filter, and the SBRs were higher (Supplementary Fig. 10c and 10d). Thanks to an obvious tail to 1400 nm of TT3-*o*CB molecule, the exposure time of imaging was 50 ms in this study, which ensures the framerate smooth and satisfies the requirements of surgery. It demonstrated that, in the brightness of fluorescent probe permitting, NIR-II imaging beyond 1400 nm wavelength was a better modality for imaging-guided surgery.

We also applied this hybrid navigation mode in mouse tumor model with metastatic LNs. Luciferase-transfected 4T1 cells were injected into the foreleg foot pad of nude mouse. After 7 days, the axillary lymph node was found obvious luciferase signals. The AIE cocktail was then injected into the paracancerous tissues. We could find NIR-II fluorescence in metastatic LNs. Under the guidance of NIR-II imaging, we incised the skin and detected the visible fluorescence. With the navigation of strong visible fluorescence, the metastatic LN was completely resected and verified no residue (Supplementary Figure 11).

3.4. The NIR-II and visible fluorescence hybrid surgical navigation mode can facilitate surgeries both in LN and other systems

Validating the efficiency of one medical technique in large-bodied animal is important for pre-clinical evaluation, especially for surgical navigation systems. To further explore the potential application of this hybrid surgical navigation mode, we then selected rabbits as our animal model and visualized the mesenteric lymph nodes, ureter and bile ducts in both NIR-II window and visible light region. Our home-built NIR-II fluorescence imaging system could offer a sufficiently large field of view

through regulating the electric lifting platform (Fig. 4a). Studies exploring the efficiency of AIE fluorescent nanoprobes-assisted surgery in rabbit model were limited [31,35], and no previous study explored it in mesenteric lymph nodes in rabbit. We injected the nanoprobe cocktail into the wall of small intestine at three sites (Fig. 4b). Although the mesenteric LNs were difficult to be distinguished in bright field (Fig. 4c), they could be rapidly detected in the NIR-II fluorescence channel 10 min after injection (Fig. 4d, red circle). The whole lymphatic vascular network distributing along with blood vessels were also rapidly presented in the mesenteries (Fig. 4d, white arrow). Under the excitation of ultraviolet light, the LN could be carefully resected guided by both NIR-II and visible fluorescence imaging (Fig. 4e). The resected LN was confirmed by pathological section and H&E staining (Supplementary Figure 12).

Iatrogenic extrahepatic bile duct injury is one of most troublesome complications in the up-abdominal surgery, such as cholecystectomy [36]. It could lead to biliary fistula, abdominal sepsis, biliary obstruction and repeated surgery [36]. A small percentage of patients might suffer from a dismal prognosis and need liver transplantation [37]. Currently, cholangiography based on X-ray imaging was widely used in clinical practice to prevent iatrogenic bile duct injury [36]. However, potential radiation damage and large-sized cumbersome equipment made this intraoperative examination unfriendly to surgeons. Fluorescence techniques was a nonradioactive strategy to realize intraoperative cholangiography. Our previous study reported that NIR-II imaging technique could be a promising method for cholangiography [35]. We then applied our novel fluorescence hybrid surgical navigation mode in extrahepatic bile ducts imaging (Fig. 4f). After laparotomy, the hepatic hilar region was exposed, and the duodenal papilla was carefully identified. The nanoprobes cocktail was retrogradely injected into the bile ducts through duodenal papilla. In the bright field, the extrahepatic bile ducts were hard to be detected, and many blood vessels crossed on extrahepatic bile duct (Fig. 4g). In NIR-II imaging, the whole extrahepatic bile ducts were clearly visualized (Fig. 4h). Under the excitation of ultraviolet lamp, we could also easily distinguish the extrahepatic bile duct with bright orange fluorescence (Fig. 4i). Interestingly, a branch of bile duct was occluded by soft tissues according to the visible fluorescence channel (Figs. 4i–1, red rectangle), whereas it could be clearly observed in the NIR-II fluorescence image (Fig. 4h, red rectangle). After the branch of bile duct was carefully dissected under the assistance of NIR-II imaging and guidance of visible fluorescence, the full view of this branch was presented without injury (Figs. 4i–2).

Also, iatrogenic ureteral injury is a dreaded complication which can lead to intra-abdominal infection, urethral stricture, renal failure and second surgery. [38–40]. In general, because identifying ureters during surgeries mainly base on the experience of surgeons, unexpected ureteral injury is therefore difficult to be thoroughly avoided. With the development of NIR imaging technique, surgeons recently applied this technique in intraoperative detection of ureters and decreased the injury rate. [41]. Considering the better performance of fluorescence imaging in NIR-II region, we further verified the application value of this new hybrid fluorescence navigation mode in urinary system. The retroperitoneal area was exposed after laparotomy, and the mixed tracers were injected into renal pelvis (Fig. 4j). Ureter was not easily detected in bright field, but could be sufficiently visualized in NIR-II region (Fig. 4k and l). We could also observe the whole ureter with bright orange fluorescence under ultraviolet excitation (Fig. 4m). However, in the thick tissues or under the blood vessels, the visible fluorescence could not penetrate those tissues and need the complementary guidance of NIR-II imaging (Fig. 4m, red rectangle).

3.5. The advantages of the NIR-II and visible fluorescence hybrid surgical navigation mode

To fully exhibit the advantages of this hybrid navigation mode, we first compared the operative time between NIR-II fluorescence imaging-

guided surgery and hybrid navigation surgery. The left fore-footpad was injected with TT3-*o*CB NPs, and the right one was injected with the NPs cocktail (Fig. 5a). Ten minutes after injection, the left axillary LN resection was only guided by NIR-II fluorescence imaging, whereas the right axillary LN resection was guided by hybrid surgical navigation mode. We recruited six surgeons as volunteers and fully informed this project to them. Two of them were in authorship, and rest four surgeons were not. The volunteers had 1 to 8 years-surgical experiences, and the detailed information was listed in Fig. 5b. Our result showed that the operations guided by hybrid surgical navigation mode were less time consuming than that guided merely by NIR-II fluorescence for all the six surgeons (Fig. 5c). The mean operative time was 32.8 s in hybrid fluorescence guided surgery group, which was much shorter than that in NIR-II imaging guided surgery group (90.6 s). Human eyes could not respond to the NIR-II fluorescence. When performing a NIR-II imaging guided surgery, we relied on an InGaAs camera and observed images in the screen. Because the NIR-II signals were not in the surgical field, it demanded a higher hand-eye coordination and a longer learning curve for surgeons. However, the hybrid navigation mode combined the merits of NIR-II fluorescence imaging and visible fluorescence imaging. NIR-II imaging helped surgeons to detect the targeted lesions buried deep in tissues and offered images with higher resolution. After incising the skin, the targeted tissues with visible fluorescence could be detected by naked eyes and resected more conveniently. Our study solved problem of hand-eye coordination during surgery from fluorescent probes dimension. Another potentially alternative solution to solve this problem was from device dimension. The representative device was fluorescence goggle system, a kind of head-mounted NIR detector established by Achilefu and co-workers. [42]. However, for NIR-II fluorescent imaging, the current InGaAs detector was too heavy to wear on the head.

Another advantage of this new hybrid mode was that it could integrate NIR-II fluorescence macroscopic imaging and visible fluorescence endoscopic imaging (Fig. 5d and f). Nowadays, resection of diseased lesions is not the only purpose of surgery. Surgeons also should take minimal invasion and cosmetic appearance into consideration. For some surgeries, such as breast surgery, thyroid surgery and superficial lymph node biopsy, surgeons could hide the surgical incision in hidden site or reduce the length of incision under the assistance with endoscopy. [43, 44]. For example, minimally invasive video-assisted thyroidectomy (MIVAT) was proven as a safe and effective surgery since its introduction in the late 1990s. [43]. These kinds of surgeries for superficial organs, combining open operations and endoscopic operations, could benefits from our new hybrid navigation mode. Firstly, we verified this concept in EP tube filled with NPs cocktail *in vitro*. The visible-light endoscopic system was modified by adding a 400 nm long-pass filter and a 750 nm short-pass filter and introducing a 390 nm laser into system (Fig. 5f). Strong NIR-II fluorescent signal could be detected by InGaAs camera (Fig. 5e, left), and bright visible fluorescence could be detected by visible-light endoscopy (Fig. 5g and h, left). We established a rat model as a sample demo to demonstrate the potential application value of hybrid navigation mode in endoscopy-assisted surgery. A rat was anesthetized and received laparotomy. Then, a segment of small intestine was selected and ligated at both proximal and distal sites (Supplementary Figure 13a). We further injected the NPs cocktail into the intestinal segment, replaced this intestinal segment into rat"s abdominal cavity and sutured abdominal wall (Supplementary Figure 13b). The selected segment of intestine could be visualized clearly and directly in NIR-II fluorescence channel (Fig. 5e, right), which helped us locate the targeted tissues in abdominal cavity. After performing a small incision, we could use our home-modified endoscope to observe the intestine segment in bright field and the bright fluorescence under the excitation of 390 nm laser (Fig. 5g and h, right).

3.6. An alternatively feasible strategy for currently clinical practice

Although the above-mentioned AIE nanoprobes cocktail exhibited

excellent mechanical properties and high biological compatibility, it remains a relatively long way to apply them in clinical practice. To achieve the NIR-II and visible fluorescence imaging-guided surgery in currently clinical practice, we proposed an alternative strategy as a compromise. Berberine chloride was a widely used antibiotic for treating diarrhea, [45], and proved to be an antitumor agent recently. [46]. Our previous study has reported that berberine was an unconventional rotor-free AIE agent. [47]. Considering the safety of berberine has been comprehensively validated, we selected this old drug as a candidate for imaging-guided surgery. In this study, we found berberine had a limited solubility in water which limited its clinical use. Therefore, β-cyclodextrin, an FDA-approved agent, was used to form a host-guest complex with berberine to increase its solubility according to previously published method (Fig. 6a). [48]. Because of the restriction of berberine molecular motion by (2-Hydroxypropyl)-β-cyclodextrin, this host-guest complex had a significantly increased yellow fluorescence under the excitation of ultraviolet light (Supplementary Figure 14). The absorption peak and emission peak of berberine were 340 nm and 565 nm, respectively (Fig. 6b). In addition, we found that the fluorescence of berberine could be further enhanced by albumin in plasma (Supplementary Figure 15). ICG was an FDA-approved NIR fluoroprobe with emission peak at NIR-I region (Fig. 6c and d). Recent studies began to evaluate the application value of NIR-II imaging technique in surgical navigation, using ICG"s intense tail signal in NIR-II region. [13,49]. Since the solubility of ICG obviously decreased in salt solution, much precipitate was observed when ICG was added into berberine solution (Supplementary Figure 15). We therefore added 2% bovine serum albumin (BSA) in the solvent system to increase the solubility of ICG (Supplementary Figure 16). In further clinical practice, BSA could be replaced by human serum albumin or patients" plasma. The *in vitro* performance of berberine and ICG-mixed tracer was presented in Fig. 6e. Both bright yellow fluorescence and strong NIR-II signals of mixed tracer could be obtained under different excitation conditions (Fig. 6e).

Animal experiments were further performed. We first used a mouse model to explore the performance of berberine and ICG mixed tracer. The mixed tracer was injected into the hindlimb footpad of an ICR mouse (Fig. 6f–i), and the popliteal LN could be detected 5 min minutes after injection using InGaAs camera (Fig. 6f–ii). Then, we incised the skin and exposed the LN under the guidance of yellow fluorescence from berberine (Fig. 6f–iii). Similar procedure was performed in rat. The mixed tracer was injected into forelimb footpad (Fig. 6g–i). We could directly detect the axillary LN in NIR-II biological window (Fig. 6g–ii), and observe the yellow fluorescence after incising skin (Fig. 6g–iii). At last, a rabbit model was used to access the application potential in breast sentinel LN. A female rabbit was selected, and its breast was injected with mixed tracer (Fig. 6h–i). Fifteen minutes after injection, the sentinel LN was visualized clearly using NIR-II imaging system (Fig. 6h and ii). We further incised the skin, and strong yellow fluorescence could be obtained and guided us to perform lymphadenectomy (Fig. 6h and iii).

However, this alternative strategy had its own drawbacks. We found that small molecules, such as ICG, were easily leaked into blood vessels (Supplementary figure 17a) and rapidly captured by liver or kidney (Supplementary figure 17b), which consisted with our previous study. [26]. This neglected phenomenon could also be observed in other studies. [30,50]. Tian et al. compared the performance of LN labeling between quantum dots and ICG. The obvious NIR-II fluorescent signals from liver region were detected in ICG group, whereas no NIR-II fluorescence was detected in QDs group. [50]. The fluorescent signals outside the LN undoubtedly bring interference into imaging-guided surgery. Moreover, such small contrast agents were taken up and transported quickly through the lymphatic vessels, [51], which led to a short observation time in discriminating SLNs from next tier nodes. At last, as we above-mentioned, NIR-II fluorescence imaging beyond 1400 nm wavelength had a better imaging performance. However, the fluorescence intensity of ICG beyond 1400 nm could not satisfy the requirement of surgery. Hence, more fluorescent probes with excellent optical
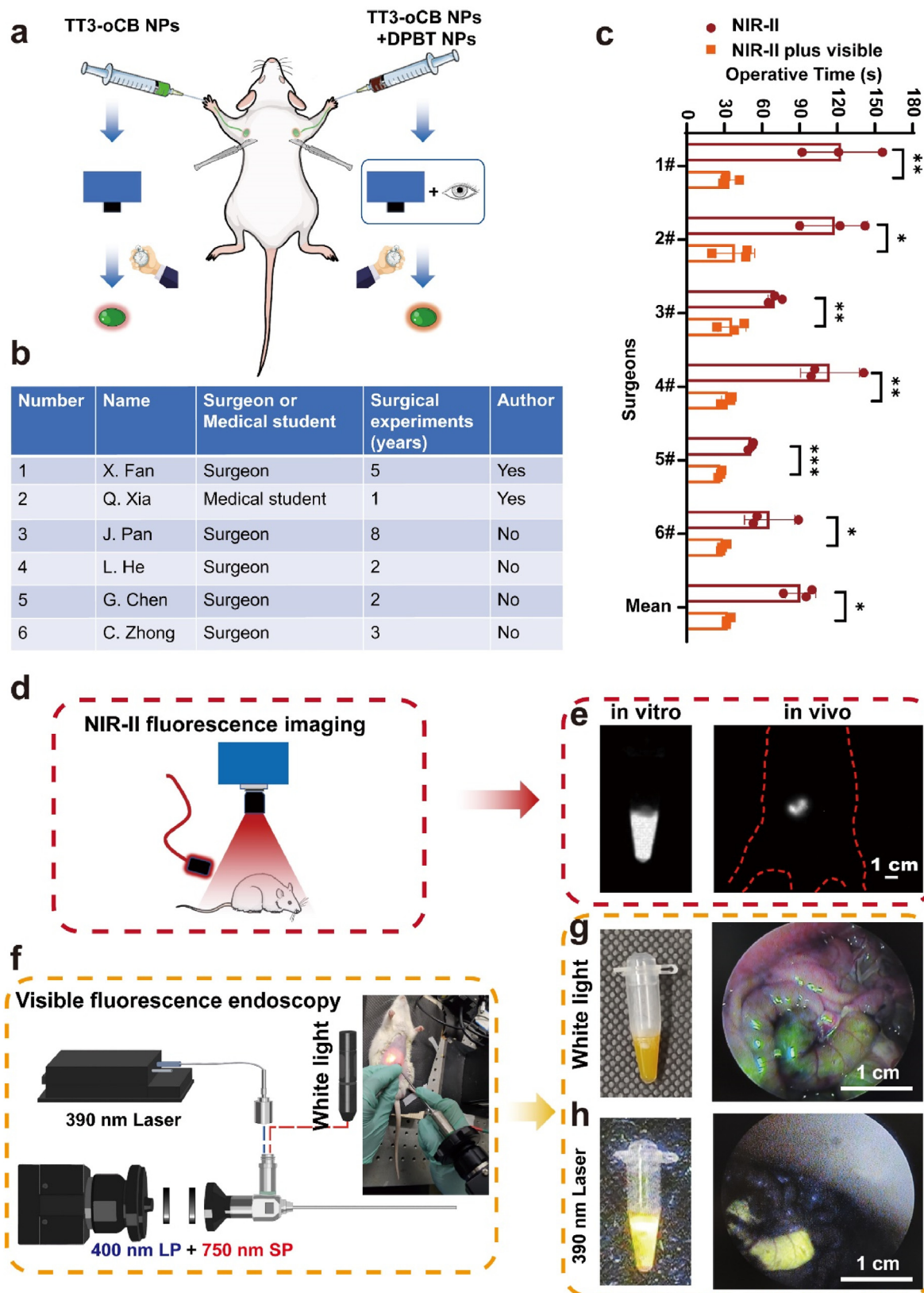
Fig. 5. a) Schematic of the comparison between two types of imaging-guided surgeries. **b)** Information of volunteers. **c)** The lengths of operative time for two surgical modes. **d)** Schematic diagram of NIR-II fluorescence imaging system. **e)** NIR-II fluorescence imaging of the EP tube and selected segment of intestine (scale bar: 1 cm). **f)** Schematic of the home-modified endoscopic system. **g)** Morphology of the EP tube and segment of intestine in bright field. **h)** Visible fluorescence images of the EP tube and segment of intestine observed by endoscopy. All values are mean ± S.E.M (n = 3), *p < 0.05, **p < 0.01, ***p < 0.001.
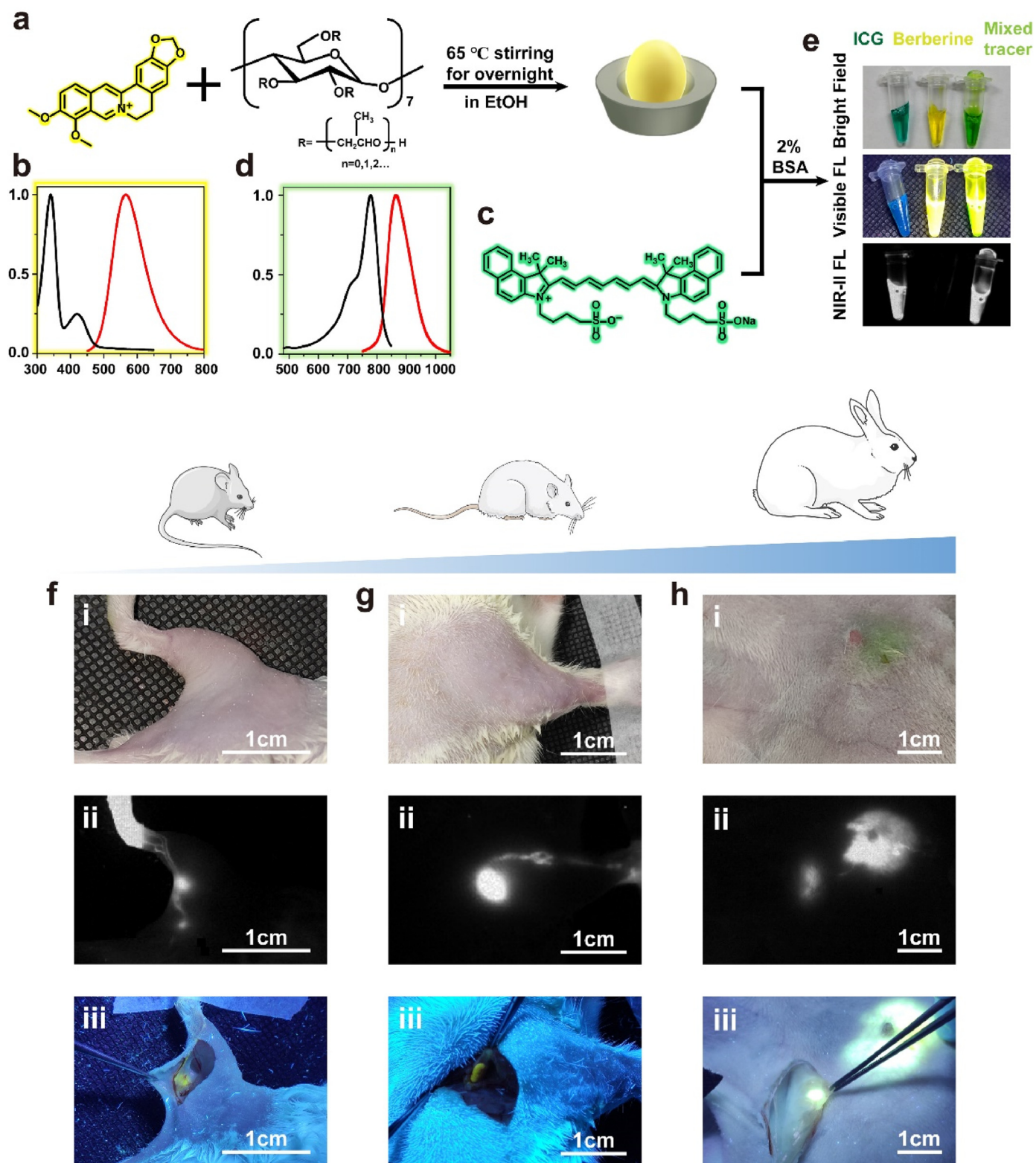
Fig. 6. a) Schematic representations of berberine coated with (2-Hydroxypropyl)- β-cyclodextrin. **b)** The absorption and emission spectra of berberine@(2-Hydroxypropyl)-β-cyclodextrin. **c)** The chemical formula of ICG. **d)** The absorption and emission spectra of ICG solution. **e)** Comparison of the *in vitro* performance of ICG, berberine, and mixture, under different excitation conditions. The performances of the mixed tracer **f)** in an ICR mouse, **g)** in a rat and **h)** in a rabbit (scale bar: 1 cm). NIR-II imaging condition: 1100 long-pass filter, exposure time, 10 ms; power intensity, 15 mW/cm².

properties, such as AIE materials, novel small molecular fluorophores, are urgent in clinical demands. Not only synthesizing all kinds of different fluorophores, but also developing novel navigation modes and clinical translational research, should be paid particular attention to.

4. Conclusions

In this work, we proposed a NIR-II and visible fluorescence hybrid navigation mode using a NIR-II fluorescent AIE probe and a visible

fluorescent AIE probe. The cocktail of AIE NPs could help to locate the targeted lesions or organs (e.g. lymph nodes, ureters, bile duct et al.) in deep tissues by NIR-II imaging and resect them under the guidance of visible fluorescence. This hybrid navigation mode could not only accelerate the speed of imaging-guided surgery, but also potentially integrate with the fluorescence endoscope. We also suggested that the standard hybrid navigation surgery should include six steps. To better understand the mechanism of LN labeling, we firstly deciphered the distribution of NPs in LN by a NIR-II fluorescence wide-scope microscope and showed two fates of NPs in LNs after local injection. At last, an alternative strategy which combined ICG and berberine was presented. Both two agents were clinically approved and had the potential for rapidly clinical translation. This novel navigation mode provided a promising and potentially translational strategy to the precision surgery.

Credit aAuthor sStatement

Conceptualization: J. Qian, H. Lin, X. Fan; Methodology: X. Fan, Q. Xia, S. Liu, Z. Zheng, G. Tang; Investigation: X. Fan, Q. Xia, S. Liu, Z. Zheng, Y. Zhang, Y. Li; Visualization: X. Fan, Q. Xia; Supervision: B.Z. Tang, J. Qian, H. Lin; Writing – original draft: X. Fan, Q. Xia; Writing – review & editing: X. Fan, Y. Zhang.

Funding sources

Declaration of competing interest

The authors declare that they have no known competing financial interests or personal relationships that could have appeared to influence the work reported in this paper.

Acknowledgements

Appendix A. Supplementary data

Supplementary data to this article can be found online at https://doi.org/10.1016/j.mtbio.2022.100399.

References

[1] J. Dong, N. Zhang, [Precise surgery], Zhonghua Wai Ke Za Zhi 53 (2015) 321–323.
[2] J. Dong, X. Qi, Liver imaging in precision medicine, EBioMedicine 32 (2018) 1–2.
[3] Z. Zhang, K. He, C. Chi, Z. Hu, J. Tian, Intraoperative fluorescence molecular imaging accelerates the coming of precision surgery in China, Eur. J. Nucl. Med. Mol. Imag. 49 (8) (2022) 2531–2543.
[4] E.M. Walsh, D. Cole, K.E. Tipirneni, K.I. Bland, N. Udayakumar, B.B. Kasten, S.L. Bevans, B.M. McGrew, J.J. Kain, Q.T. Nguyen, E.L. Rosenthal, J.M. Warram, Fluorescence imaging of nerves during surgery, Ann. Surg. 270 (2019) 69–76.
[5] J.S.D. Mieog, F.B. Achterberg, A. Zlitni, M. Hutteman, J. Burggraaf, R.-J. Swijnenburg, S. Gioux, A.L. Vahrmeijer, Fundamentals and developments in fluorescence-guided cancer surgery, Nat. Rev. Clin. Oncol. 19 (2022).
[6] Q.Y. Chen, J.W. Xie, Q. Zhong, J.B. Wang, J.X. Lin, J. Lu, L.L. Cao, M. Lin, R.H. Tu, Z.N. Huang, J.L. Lin, H.L. Zheng, P. Li, C.H. Zheng, C.M. Huang, Safety and efficacy of indocyanine green tracer-guided lymph node dissection during laparoscopic radical gastrectomy in patients with gastric cancer: a randomized clinical trial, JAMA Surg 155 (4) (2020) 300–311.
[7] V.M. Moncayo, A.L. Alazraki, N.P. Alazraki, J.N. Aarsvold, Sentinel lymph node biopsy procedures, Semin. Nucl. Med. 47 (2017) 595–617.
[8] Z. Wang, X. Yang, J. Wang, P. Liu, Y. Pan, C. Han, J. Pei, Real-time navigation system with indocyanine green fluorescence for sentinel lymph node biopsy in patients with breast cancer, Front. Oncol. 11 (2021), 621914.
[9] Z. Feng, T. Tang, T. Wu, X. Yu, Y. Zhang, M. Wang, J. Zheng, Y. Ying, S. Chen, J. Zhou, X. Fan, D. Zhang, S. Li, M. Zhang, J. Qian, Perfecting and extending the near-infrared imaging window, Light Sci. Appl. 10 (2021) 197.
[10] K. Welsher, Z. Liu, S.P. Sherlock, J.T. Robinson, Z. Chen, D. Daranciang, H. Dai, A route to brightly fluorescent carbon nanotubes for near-infrared imaging in mice, Nat. Nanotechnol. 4 (2009) 773–780.
[11] G. Hong, J.C. Lee, J.T. Robinson, U. Raaz, L. Xie, N.F. Huang, J.P. Cooke, H. Dai, Multifunctional in vivo vascular imaging using near-infrared II fluorescence, Nat. Med. 18 (2012) 1841–1846.
[12] Y. Zhang, G. Hong, Y. Zhang, G. Chen, F. Li, H. Dai, Q. Wang, Ag2S quantum dot: a bright and biocompatible fluorescent nanoprobe in the second near-infrared window, ACS Nano 6 (2012) 3695–3702.
[13] Z. Hu, C. Fang, B. Li, Z. Zhang, C. Cao, M. Cai, S. Su, X. Sun, X. Shi, C. Li, T. Zhou, Y. Zhang, C. Chi, P. He, X. Xia, Y. Chen, S.S. Gambhir, Z. Cheng, J. Tian, First-in-human liver-tumour surgery guided by multispectral fluorescence imaging in the visible and near-infrared-I/II windows, Nat Biomed Eng 4 (2020) 259–271.
[14] C. Cao, Z. Jin, X. Shi, Z. Zhang, A. Xiao, J. Yang, N. Ji, J. Tian, Z. Hu, First clinical investigation of near-infrared window IIa/IIb fluorescence imaging for precise surgical resection of gliomas, IEEE Trans. Biomed. Eng. 69 (8) (2022) 2404–2413.
[15] M. Zhang, J. Yue, R. Cui, Z. Ma, H. Wan, F. Wang, S. Zhu, Y. Zhou, Y. Kuang, Y. Zhong, D.W. Pang, H. Dai, Bright quantum dots emitting at approximately 1,600 nm in the NIR-IIb window for deep tissue fluorescence imaging, Proc. Natl. Acad. Sci. U. S. A. 115 (2018) 6590–6595.
[16] M. Yu, X. Yang, Y. Zhang, H. Yang, H. Huang, Z. Wang, J. Dong, R. Zhang, Z. Sun, C. Li, Q. Wang, Pb-doped Ag Se quantum dots with enhanced photoluminescence in the NIR-II window, Small 17 (2021), e2006111.
[17] M. Kamimura, T. Matsumoto, S. Suyari, M. Umezawa, K. Soga, Ratiometric near-infrared fluorescence nanothermometry in the OTN-NIR (NIR II/III) biological window based on rare-earth doped beta-NaYF4 nanoparticles, J. Mater. Chem. B 5 (2017) 1917–1925.
[18] N. Alifu, A. Zebibula, J. Qi, H. Zhang, C. Sun, X. Yu, D. Xue, J.W.Y. Lam, G. Li, J. Qian, B.Z. Tang, Single-molecular near-infrared-II theranostic systems: ultrastable Aggregation-induced emission nanoparticles for long-term tracing and efficient photothermal therapy, ACS Nano 12 (2018) 11282–11293.
[19] X. Liu, Y.Y. Yang, M.J. Ling, R. Sun, M.Y. Zhu, J.J. Chen, M. Yu, Z.W. Peng, Z.Q. Yu, X.Q. Liu, Near-infrared II light-triggered robust carbon radical generation for combined photothermal and thermodynamic therapy of hypoxic tumors, Adv. Funct. Mater. 31 (2021).
[20] J. Luo, Z. Xie, J.W. Lam, L. Cheng, H. Chen, C. Qiu, H.S. Kwok, X. Zhan, Y. Liu, D. Zhu, B.Z. Tang, Aggregation-induced emission of 1-methyl-1,2,3,4,5-pentaphenylsilole, Chem. Commun. (2001) 1740–1741.
[21] Q. Xia, Y. Zhang, Y. Li, Y. Li, Y. Li, Z. Feng, X. Fan, J. Qian, H. Lin, A historical review of aggregation-induced emission from 2001 to 2020: a bibliometric analysis, Aggregate 3 (2022) e152.
[22] Z. Wang, L. Yu, Y. Wang, C. Wang, Q. Mu, X. Liu, M. Yu, K.-N. Wang, G. Yao, Z. Yu, Dynamic adjust of non-radiative and radiative attenuation of AIE molecules reinforces NIR-II imaging mediated photothermal therapy and immunotherapy, Adv. Sci. 9 (2022), e2104793.
[23] X. Cai, K.-N. Wang, W. Ma, Y. Yang, G. Chen, H. Fu, C. Cui, Z. Yu, X. Wang, Multifunctional AIE iridium (III) photosensitizer nanoparticles for two-photon-activated imaging and mitochondria targeting photodynamic therapy, J. Nanobiotechnol. 19 (2021) 254.
[24] J. Mei, N.L.C. Leung, R.T.K. Kwok, J.W.Y. Lam, B.Z. Tang, Aggregation-induced emission: together we shine, united we soar, Chem. Rev. 115 (2015) 11718–11940.
[25] P. Wang, Y. Fan, L. Lu, L. Liu, L. Fan, M. Zhao, Y. Xie, C. Xu, F. Zhang, NIR-II nanoprobes in-vivo assembly to improve image-guided surgery for metastatic ovarian cancer, Nat. Commun. 9 (2018) 2898.
[26] X.X. Fan, Y.R. Li, Z. Feng, G.Q. Chen, J. Zhou, M.B. He, L. Wu, S.L. Li, J. Qian, H. Lin, Nanoprobes-assisted multichannel NIR-II fluorescence imaging-guided resection and photothermal ablation of lymph nodes, Adv. Sci. 8 (2021) 13.
[27] S. Liu, R. Chen, J. Zhang, Y. Li, M. He, X. Fan, H. Zhang, X. Lu, R.T.K. Kwok, H. Lin, J.W.Y. Lam, J. Qian, B.Z. Tang, Incorporation of planar blocks into twisted skeletons: boosting brightness of fluorophores for bioimaging beyond 1500 nanometer, ACS Nano 14 (2020) 14228–14239.
[28] Z. Zheng, H. Zhang, H. Cao, J. Gong, M. He, X. Gou, T. Yang, P. Wei, J. Qian, W. Xi, B.Z. Tang, Intra- and intermolecular synergistic engineering of aggregation-induced emission luminogens to boost three-photon absorption for through-skull brain imaging, ACS Nano (2022). Online published.
[29] D. Li, S. He, Y. Wu, J. Liu, Q. Liu, B. Chang, Q. Zhang, Z. Xiang, Y. Yuan, C. Jian, A. Yu, Z. Cheng, Excretable lanthanide nanoparticle for biomedical imaging and surgical navigation in the second near-infrared window, Adv. Sci. 6 (2019), 1902042.
[30] A. Cousins, S.K. Thompson, A.B. Wedding, B. Thierry, Clinical relevance of novel imaging technologies for sentinel lymph node identification and staging, Biotechnol. Adv. 32 (2014) 269–279.
[31] D. Zhong, W. Chen, Z. Xia, R. Hu, Y. Qi, B. Zhou, W. Li, J. He, Z. Wang, Z. Zhao, D. Ding, M. Tian, B.Z. Tang, M. Zhou, Aggregation-induced emission luminogens for image-guided surgery in non-human primates, Nat. Commun. 12 (2021) 6485.

[32] X. Fan, Q. Xia, Y. Zhang, Y. Li, Z. Feng, J. Zhou, J. Qi, B.Z. Tang, J. Qian, H. Lin, Aggregation-induced emission (AIE) nanoparticles-assisted NIR-II fluorescence imaging-guided diagnosis and surgery for inflammatory bowel disease (IBD), Adv Healthc Mater 10 (2021) e2101043.

[33] Y.-N. Zhang, J. Lazarovits, W. Poon, B. Ouyang, L.N.M. Nguyen, B.R. Kingston, W.C.W. Chan, Nanoparticle size influences antigen retention and presentation in lymph node follicles for humoral immunity, Nano Lett. 19 (2019) 7226–7235.

[34] C.J. Hughes, A.R. Shaha, J.P. Shah, T.R. Loree, Impact of lymph node metastasis in differentiated carcinoma of the thyroid: a matched-pair analysis, Head Neck 18 (1996) 127–132.

[35] D. Wu, S. Liu, J. Zhou, R. Chen, Y. Wang, Z. Feng, H. Lin, J. Qian, B.Z. Tang, X. Cai, Organic dots with large π-conjugated planar for cholangiography beyond 1500 nm in rabbits: a non-radioactive strategy, ACS Nano 15 (2021) 5011–5022.

[36] M.S. Altieri, L.M. Brunt, Elimination of bile duct injury in cholecystectomy, Adv. Surg. 53 (2019) 145–160.

[37] K.A.C. Booij, P.R. de Reuver, K. Yap, S. van Dieren, O.M. van Delden, E.A. Rauws, D.J. Gouma, Morbidity and mortality after minor bile duct injury following laparoscopic cholecystectomy, Endoscopy 47 (2015) 40–46.

[38] M. Ravlo, M.H. Moen, I.R.K. Bukholm, M. Lieng, E. Vanky, Ureteric injuries during hysterectomy-A Norwegian retrospective study of occurrence and claims for compensation over an 11-year period, Acta Obstet. Gynecol. Scand. 101 (2022) 68–76.

[39] A. Sahai, A. Ali, R. Barratt, M. Belal, S. Biers, R. Hamid, C. Harding, R. Parkinson, S. Reid, N. Thiruchelvam, British Association of Urological Surgeons (BAUS) consensus document: management of bladder and ureteric injury, BJU Int. 128 (2021) 539–547.

[40] S.M. Croghan, A. Zaborowski, H.M. Mohan, D. Mulvin, B.B. McGuire, M. Murphy, D.J. Galvin, G. Lennon, D. Quinlan, D.C. Winter, The sentinel stent? A systematic review of the role of prophylactic ureteric stenting prior to colorectal resections, Int. J. Colorectal Dis. 34 (2019) 1161–1178.

[41] W. Polom, M. Migaczewski, J. Skokowski, M. Swierblewski, T. Cwalinski, L. Kalinowski, M. Pedziwiatr, M. Matuszewski, K. Polom, Multispectral imaging using fluorescent properties of indocyanine green and methylene blue in colorectal surgery-initial experience, J. Clin. Med. 11 (2022).

[42] Y. Liu, Y.M. Zhao, W. Akers, Z.Y. Tang, J. Fan, H.C. Sun, Q.H. Ye, L. Wang, S. Achilefu, First in-human intraoperative imaging of HCC using the fluorescence goggle system and transarterial delivery of near-infrared fluorescent imaging agent: a pilot study, Transl. Res. 162 (2013) 324–331.

[43] L. Rossi, G. Materazzi, S. Bakkar, P. Miccoli, Recent trends in surgical approach to thyroid cancer, Front. Endocrinol. 12 (2021) 699805.

[44] J.D. Yang, J. Lee, J.S. Lee, E.K. Kim, C.S. Park, H.Y. Park, Aesthetic scar-less mastectomy and breast reconstruction, J Breast Cancer 24 (2021) 22–33.

[45] S. Menees, R. Saad, W.D. Chey, Agents that act luminally to treat diarrhoea and constipation, Nat. Rev. Gastroenterol. Hepatol. 9 (2012) 661–674.

[46] L. Avila-Carrasco, P. Majano, J.A. Sánchez-Toméro, R. Selgas, M. López-Cabrera, A. Aguilera, G. González Mateo, Natural plants compounds as modulators of epithelial-to-mesenchymal transition, Front. Pharmacol. 10 (2019) 715.

[47] Y. Gu, Z. Zhao, H. Su, P. Zhang, J. Liu, G. Niu, S. Li, Z. Wang, R.T.K. Kwok, X.-L. Ni, J. Sun, A. Qin, J.W.Y. Lam, B.Z. Tang, Exploration of biocompatible AIEgens from natural resources, Chem. Sci. 9 (2018) 6497–6502.

[48] H. Bai, J. Wang, C.U. Phan, Q. Chen, X. Hu, G. Shao, J. Zhou, L. Lai, G. Tang, Cyclodextrin-based host-guest complexes loaded with regorafenib for colorectal cancer treatment, Nat. Commun. 12 (2021) 759.

[49] X. Shi, Z. Zhang, Z. Zhang, C. Cao, Z. Cheng, Z. Hu, J. Tian, N. Ji, Near-infrared window II fluorescence image-guided surgery of high-grade gliomas prolongs the progression-free survival of patients, IEEE Trans. Biomed. Eng. 69 (6) (2021) 1889–1900.

[50] R. Tian, H. Ma, S. Zhu, J. Lau, R. Ma, Y. Liu, L. Lin, S. Chandra, S. Wang, X. Zhu, H. Deng, G. Niu, M. Zhang, A.L. Antaris, K.S. Hettie, B. Yang, Y. Liang, X. Chen, Multiplexed NIR-II probes for lymph node-invaded cancer detection and imaging-guided surgery, Adv. Mater. 32 (2020) e1907365.

[51] D.A. Rao, M.L. Forrest, A.W.G. Alani, G.S. Kwon, J.R. Robinson, Biodegradable PLGA based nanoparticles for sustained regional lymphatic drug delivery, J. Pharmacol. Sci. 99 (2010) 2018–2031.